

Momentum and Energy Transport by Gravity Waves in Stochastically Driven Stratified Flows. Part II: Radiation of Gravity Waves from a Gaussian Jet

NIKOLAOS A. BAKAS AND BRIAN F. FARRELL

Harvard University, Cambridge, Massachusetts

(Manuscript received 16 November 2006, in final form 19 November 2007)

ABSTRACT

Interaction between the midlatitude jet and gravity waves is examined, focusing on the nonnormality of the underlying linear dynamics, which plays an essential role in processing the wave activity and selecting structures that dominate wave momentum and energy transport. When the interior of a typical midlatitude jet is stochastically forced, waves with short horizontal wavelength are trapped inside the jet and deposit momentum and energy at jet interior critical levels. Longer waves transport momentum and energy away from the jet, and the resulting momentum flux divergence produces a significant deceleration of the tropospheric and lower-stratospheric jet. This induced drag is found to depend on the shape of the jet and on the horizontal wavelength of the excited waves, reaching a maximum at wavelength $\lambda_x = 20$ km and leading to a deceleration $O(1) \text{ m s}^{-1} \text{ day}^{-1}$ for a stochastic forcing rate of 0.1 W m^{-2} distributed over the height of the jet. This deceleration is robust to changes in static stability but is reduced when the stochastic forcing is correlated over too long a time.

Implications of gravity wave absorption for middle-atmosphere circulation are discussed, focusing on differences implied for acceleration of the winter and summer midlatitude upper-stratospheric jets. The tropospheric flow is found not only to passively filter transiting waves, but also to amplify portions of the wave spectrum in conjunction with the distributed forcing, leading to enhanced gravity wave momentum and energy fluxes in agreement with observations linking middle-atmosphere enhanced variance with regions of high jet velocities.

1. Introduction

Understanding physical mechanisms sustaining the statistical equilibrium gravity wave fluxes in the atmosphere presents a challenging problem with many practical applications including accounting for effects of gravity waves in large-scale operational models. In this two-part paper the problem of gravity wave interaction with jets is studied from the point of view of generalized stability theory (GST; Farrell and Ioannou 1996), which provides powerful tools for analysis of wave–mean flow interactions.

Specifically we investigate how a typical midlatitude jet interacts with a spectrum of waves produced by forcing within the jet. The forcing term models vorticity and thermal sources originating from a variety of physical processes such as convection, shear-induced turbu-

lence, and processes associated with adjustment toward balanced flow states. Given that these gravity wave sources have a wide range of forcing frequencies and spatial scales, we simplify and generalize our analysis and its interpretation by obtaining the response of the jet to all forcing frequencies and scales by parameterizing the forcing as white in space and time. While temporally uncorrelated forcing is idealized, it has the advantage of lacking any bias, allowing the dynamical system to select the frequencies and structures with roles in momentum and energy transport that are intrinsic to the dynamics.

In Bakas and Ioannou (2007, hereafter Part I), a simple model of a finite stably stratified shear region was studied. This model provided examples of transient growth and wave–mean flow interaction processes resulting from stochastic forcing. Shear flow was found to filter, refract, and amplify the excited waves and also to augment the wave excitation processes by transferring kinetic energy of the mean shear flow to the waves. In this second part we use GST to study a two-dimensional

Corresponding author address: Nikolaos Bakas, Geological Museum 403, 24 Oxford Street, Cambridge, MA 02138.
E-mail: nbakas@post.harvard.edu

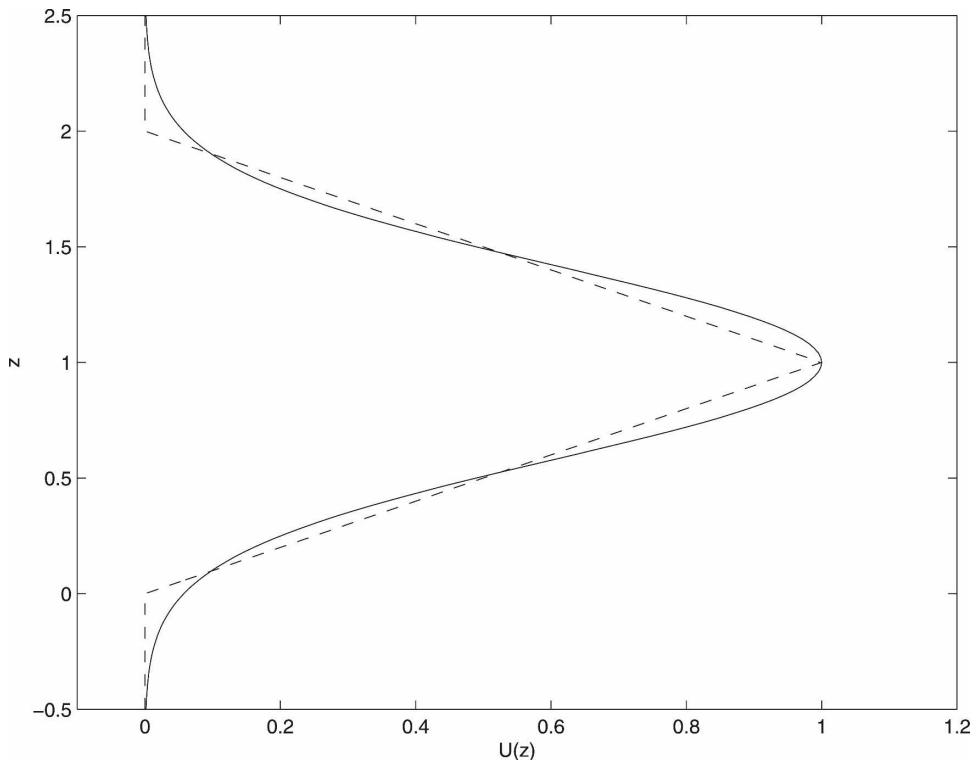


FIG. 1. Vertical velocity profile (10), where $\delta z = 0.59$. The dashed line is the profile (2) that fits the Gaussian structure with two adjacent shear layers of opposite shear.

jet focusing particularly on the perturbation-induced mean flow tendency. We find that in the statistical steady-state wave momentum flux divergence produces a significant net deceleration of the jet. This result is robust both to changes in the temporal correlation of the forcing and to changes in static stability.

This paper is organized as follows: We first obtain closed-form solutions for localized thermal excitation for both the case of a monochromatic forcing and for temporally uncorrelated forcing. We then investigate the response to forcing white in both space and time and finally examine the sensitivity of the predicted energy and momentum flux distributions to changes in the background state and in the temporal correlations of the forcing. We conclude with a discussion of our results and their implications for midlatitude jet dynamics.

2. Gravity waves produced by localized thermal forcing in a jet

The linearized, nondimensional vorticity and thermodynamic equations governing the evolution of small perturbations in a hydrostatically balanced, stratified atmosphere (cf. Part I) are

$$\left(\partial_t + \frac{U(z)}{\sqrt{\text{Ri}}} \partial_x + r(z) \right) (\nabla^2 \psi) - \frac{1}{\sqrt{\text{Ri}}} \frac{d^2 U}{dz^2} \partial_x \psi = - \frac{dr}{dz} \partial_z \psi + \partial_x \rho + \frac{1}{\text{Re}_s} \nabla^4 \psi, \quad (1a)$$

$$\left(\partial_t + \frac{U(z)}{\sqrt{\text{Ri}}} \partial_x + r(z) \right) \rho + \frac{N^2}{N_0^2} \partial_x \psi = \frac{1}{\text{Re}_s} \nabla^2 \rho, \quad (1b)$$

in which x, z are the zonal and vertical coordinates respectively, ψ is the perturbation streamfunction, and ρ is the perturbation density. The operators ∇^2 and ∇^4 are defined as $\nabla^2 = \partial^2/\partial x^2 + \partial^2/\partial z^2$ and $\nabla^4 = (\nabla^2)^2$, respectively. The Richardson number is $\text{Ri} = N_0^2 H^2 / V_0^2$, the Reynolds number is $\text{Re}_s = \rho_m H^2 N_0 / \mu$, where μ is the coefficient of viscosity, and H, V_0 , and N_0 are characteristic values of length, velocity, and inverse time, taken to be the tropopause height $H = 10$ km, a characteristic jet speed $V_0 = 30 \text{ m s}^{-1}$ and $N_0 = 0.012 \text{ s}^{-1}$, respectively, yielding Richardson number $\text{Ri} = 16$. The Brunt-Väisälä frequency, N , is constant and equal to its characteristic value N_0 , unless stated otherwise. The Rayleigh damping $r(z)$ and diffusion terms are relevant to the numerical calculations presented in sections 3–5, where further details will be provided.

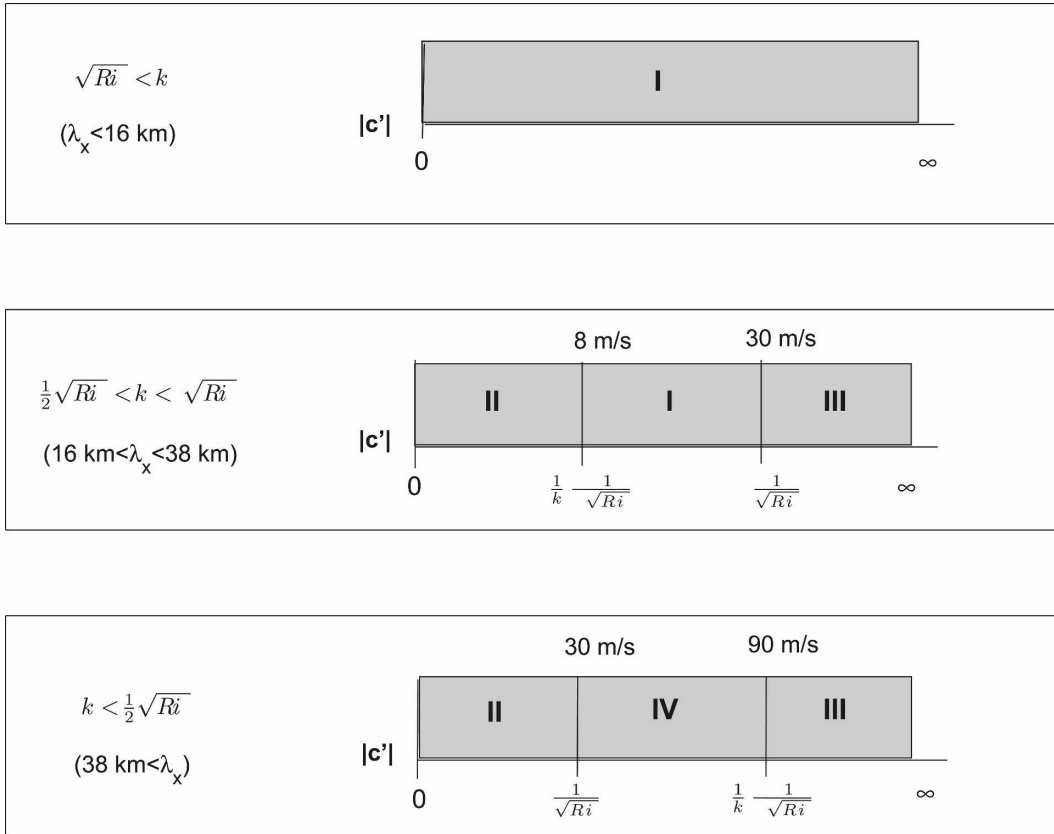


FIG. 2. Schematic representation of the dependence of propagation characteristics on the values of Ri , k , and c' . (top) For $\sqrt{Ri} \leq k$ we only have type I waves independent of the value of c' . (middle) For $(\frac{1}{2})\sqrt{Ri} < k \leq \sqrt{Ri}$ types I, II, and III exist. The numerical values seen correspond to $c' = 1/k - 1/\sqrt{Ri}$ and $c' = 1/\sqrt{Ri}$ for $\lambda_x = 20$ km ($k = \pi$) and $Ri = 16$. (bottom) For $k < (\frac{1}{2})\sqrt{Ri}$ we have only type II, III, and IV waves. The numerical values seen correspond to $c' = 1/\sqrt{Ri}$ and $c' = 1/k - 1/\sqrt{Ri}$ for $\lambda_x = 62.8$ km ($k = 1$) and $Ri = 16$.

In Part I, we saw that solving for the excitation of gravity waves by a thermal forcing harmonic in x and localized in the vertical was instructive and had the advantage of allowing a closed-form solution. To perform a similar calculation relevant to a Gaussian jet, we approximate it with the velocity profile

$$U(z) = \begin{cases} 0, & \text{for } z > 2 \\ 2 - z, & \text{for } 1 < z < 2 \\ z, & \text{for } 0 < z < 1 \\ 0, & \text{for } z < 0 \end{cases} \quad (2)$$

This profile is shown in Fig. 1. It consists of two adjacent shear layers on $0 \leq z \leq 1$ and $1 \leq z \leq 2$ with shear of opposite sign in an otherwise motionless atmosphere. The response of system (1) with this velocity profile to thermal forcing of the form $f_i(x, z, t) = \delta(z - z_\delta)e^{ikx}e^{-ikt}$, where $z_\delta = 1$ is analyzed in detail in the appendix. A qualitative description of this response follows.

The excited waves fall into four categories (hence-

forth denoted I–IV), according to the forcing frequency, the horizontal wavenumber k , and the Richardson number Ri , as sketched in Fig. 2. Type I waves have both a turning level and a critical level inside one of the shear regions. Forced waves with negative intrinsic phase speeds c' (c' is the phase speed relative to the mean flow at the forcing level) deposit their momentum at their critical levels, as shown in Fig. 3a. On the other hand waves with negative intrinsic phase speeds undergo internal reflection at turning levels and do not produce any net momentum flux (Fig. 3a).

Type II waves have a critical level but not a turning level inside the shear regions. While negative c' waves are bounded by their critical levels, type II waves with positive intrinsic phase speeds evade back reflection and escape the jet. The waves have downgradient Reynolds stress leading to energy growth that is not lost once they enter the constant velocity region as shown in Part I. To demonstrate this growth, we calculated in (A9) the outgoing energy flux $\bar{p}w$ and compared it with

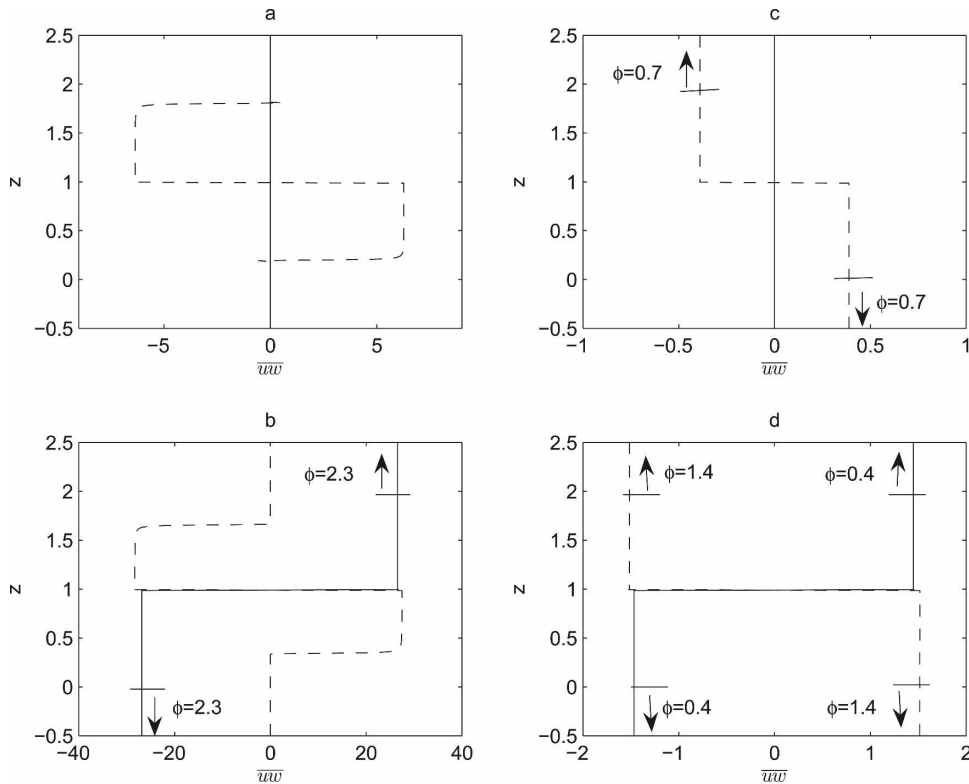


FIG. 3. Momentum flux distribution with height for the excited waves within the jet for Richardson number $Ri = 16$. (a) Type I waves that have both a turning level and a critical level inside one of the shear regions. The cases shown are waves with phase velocity $c' = 0.2$ (solid line) and $c' = -0.2$ (dashed line). The zonal wavenumber is $k = 3$. (b) Type II waves that have a critical level but no turning level. The cases shown are waves with phase velocity $c' = 0.16$ (solid line) and $c' = -0.16$ (dashed line). The zonal wavenumber is $k = 1$. (c) Type III waves that have a turning level but not a critical level inside the jet. The cases shown are waves with phase velocity $c' = 0.8$ (solid line) and $c' = -0.8$ (dashed line). The zonal wavenumber is $k = 1$. (d) Type IV waves that have neither a critical nor a turning level inside the jet. The cases shown are waves with phase velocity $c' = 0.44$ (solid line) and $c' = -0.44$ (dashed line). The zonal wavenumber is $k = 1$. Noted in (b), (c), and (d) are the outgoing energy fluxes, ϕ , scaled by the outgoing fluxes in the case of uniform flow.

the corresponding flux \overline{pw}_0 obtained in an equally forced unsheared flow. The ratio $\phi = \overline{pw}/\overline{pw}_0 = 2.3$ for the waves having $c' = 0.16$ is shown in Fig. 3b.

Type III waves have a turning level but not a critical level inside the shear region, and their momentum and energy flux transport are shown in Fig. 3c. Since the Reynolds stress is upgradient for these waves, they lose a part of their energy to the mean flow ($\phi = \overline{pw}/\overline{pw}_0 = 0.7 < 1$). The rest of the type III waves ($c' > 0$) are ducted inside the jet waveguide and do not contribute to the momentum flux budget (Fig. 3c).

Finally, type IV waves having neither a turning nor a critical level inside the shear region transport energy and momentum away from the jet as shown in Fig. 3d.

We now extend the above analysis by considering temporally uncorrelated stochastic forcing distributed over a narrow region near the jet maximum:

$$f_l(x, z, t) = e^{ikx} \frac{1}{\alpha\sqrt{\pi}} e^{-[(z-z_\delta)^2/\alpha^2]} \eta(t), \quad (3)$$

where $z_\delta = 1$ and $\eta(t)$ is a δ correlated white-noise process. The vertical distribution of the forcing has the form of a sharp Gaussian ($\alpha = 0.025$) which retains the vertical localization of the delta function while avoiding the divergence of input variance as $\omega \rightarrow 0$ implied by the Gaussian distribution.¹ The ensemble mean momentum and energy fluxes for such localized forcing are given to a good approximation by

¹ This is the ‘‘infrared catastrophe’’ problem, appearing when the forcing has a delta function form in the vertical, and was also discussed in Part I.

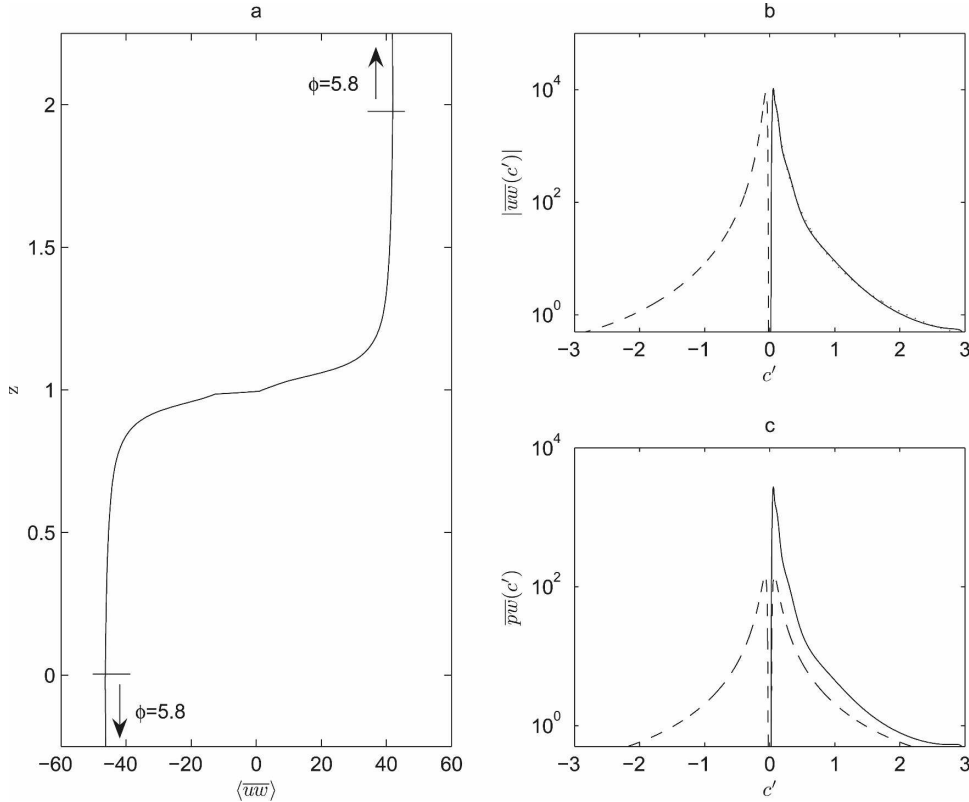


FIG. 4. (a) The ensemble mean momentum flux $\langle \overline{u\overline{w}} \rangle$ as a function of height for forcing uncorrelated in time and for velocity profile (2). The Richardson number is $\text{Ri} = 16$; the zonal wavenumber is $k = 1 < (1/2)\sqrt{\text{Ri}}$. The outgoing ensemble mean energy flux $\langle \overline{p\overline{w}} \rangle$ calculated at $z = 0$, $z = 2$ and scaled by the corresponding flux $\langle \overline{p\overline{w}_0} \rangle$ for an atmosphere at rest is denoted by ϕ . Also shown is the resulting distribution of the absolute value of (b) momentum flux and (c) energy flux at $z = 1.5$ across wave phase speeds for $\text{Ri} = 16$ and $k = 1$. The corresponding distribution of fluxes for a motionless atmosphere is also plotted (dashed lines) for reference.

$$[\langle \overline{u\overline{w}} \rangle, \langle \overline{p\overline{w}} \rangle] = \int_{-\infty}^{\infty} [\overline{u\overline{w}}(\omega), \overline{p\overline{w}}(\omega)] \hat{f} \hat{f}^* d\omega, \quad (4)$$

where

$$\begin{aligned} \hat{f} &= \frac{1}{\sqrt{2\pi}} \int_{-\infty}^{\infty} \frac{1}{\alpha\sqrt{\pi}} e^{-[(z-z_f)^2/\alpha^2]} e^{-ilz} dz \\ &= \frac{1}{\sqrt{2\pi}} e^{-l^2\alpha^2/4} = \frac{1}{\sqrt{2\pi}} e^{-(k^2\text{Ri}/\omega^2 - k^2)\alpha^2/4}, \end{aligned} \quad (5)$$

and $\overline{u\overline{w}}(\omega)$, $\overline{p\overline{w}}(\omega)$ are given by (A8) and (A9) in the appendix, respectively. The flux $\langle \overline{u\overline{w}} \rangle$ as a function of height is plotted in Fig. 4a for $\text{Ri} = 16$ and $k = 1$.

Although temporally uncorrelated forcing equally excites all frequencies, the dynamics respond primarily at low intrinsic frequencies, corresponding also to low intrinsic phase speeds (A2). Therefore type II waves, which have low intrinsic phase speeds as illustrated in

the middle and lower panels of Fig. 2, dominate the response. The large peak of $\overline{u\overline{w}}$ and $\overline{p\overline{w}}$ for low phase speeds, plotted in Figs. 4b,c, is attributed to type II waves with $c' > 0$. These waves induce a transport of westerly momentum upward and easterly momentum downward (Fig. 4a), accompanied by a large radiated energy flux ($\phi = 4$) compared to the equally forced motionless atmosphere case due to amplification of these waves inside the jet. On the other hand, the absence in the spectrum of waves with negative intrinsic frequencies can be traced to critical-level filtering and mean wind ducting of these waves, which results in deposition of their momentum inside the jet and induces the sharp increase of $\langle \overline{u\overline{w}} \rangle$ in the vicinity of $z = 1$ seen in Fig. 4a.

In Part I we found that the interaction of the forcing with the shear augmented the source of wave action provided by the forcing. To illustrate this effect for the Gaussian jet as well, we considered the temporally uncorrelated forcing given by (3), distributed over a nar-

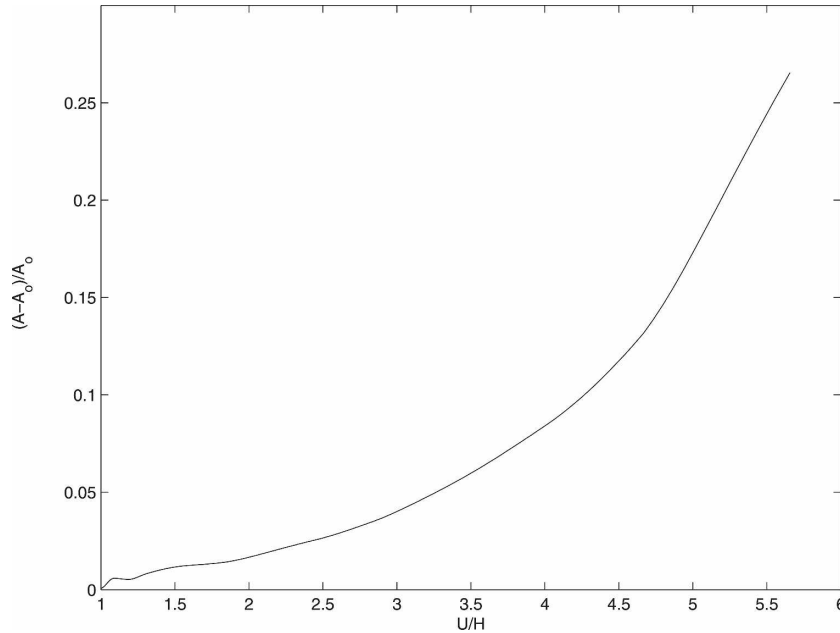


FIG. 5. Relative difference between the wave action fluxes radiated from the jet (A) and the corresponding fluxes for an equally forced motionless atmosphere (A_0) as a function of nondimensional shear. The wave action fluxes are calculated at $z = 2.5$ and integrated over all positive intrinsic phase speeds. The zonal wavenumber is $k = 1$.

row region of high mean shear ($z_\delta = 1.5$), and calculated using (4) and (A8) the emitted wave action fluxes integrated over all positive intrinsic phase speeds. Since the upward-propagating waves with $c' > 0$ are not subject to critical-level filtering, they conserve their wave action away from the forcing region. Therefore the emitted fluxes depend only on the forcing-perturbation correlation within the forcing region. As the shear increases, nonnormal growth of perturbations within the forcing region yields larger wave action fluxes compared to an equally forced motionless atmosphere as shown in Fig. 5.

Even though internal waves can penetrate beyond reflection levels if their amplitude is sufficiently large (Sutherland 2000), types I and III waves that have negative intrinsic frequencies and are ducted are not favored by the thermal forcing because of their large frequencies, and such nonlinear effects are expected to only slightly modify the results. In summary, the mean flow

augments the wave action arising from the forcing distribution and acts both as an amplifier and as a filter for the emitted waves, and these three effects together determine the features of the momentum and energy flux distributions.

3. Gravity waves produced by spatially and temporally uncorrelated forcing in a jet

We turn now to the steady-state energy and momentum fluxes resulting from stochastic excitation uncorrelated in both space and time. As in Part I, we express the perturbation Eqs. (1a) and (1b) in the compact form

$$\frac{d\mathbf{x}}{dt} = \mathbf{A}\mathbf{x} + \mathbf{F}\mathbf{f}(t), \tag{6}$$

where $\mathbf{x} = [\psi(t), \rho(t)]^T$ is the state vector discretized on grid points,

$$\mathbf{A} = \begin{cases} \nabla^{-2} \left[-\left(\frac{U}{\sqrt{\text{Ri}}} \partial_x + r \right) \nabla^2 + \frac{1}{\sqrt{\text{Ri}}} \frac{d^2 U}{dz^2} \partial_x - \frac{dr}{dz} \partial_z + \frac{1}{\text{Re}_s} \nabla^4 \right] & \nabla^{-2} \partial_x \\ -\frac{N^2}{N_0^2} \partial_x & -\left(\frac{U}{\sqrt{\text{Ri}}} \partial_x + r \right) + \frac{1}{\text{Re}_s} \nabla^2 \end{cases} \tag{7}$$

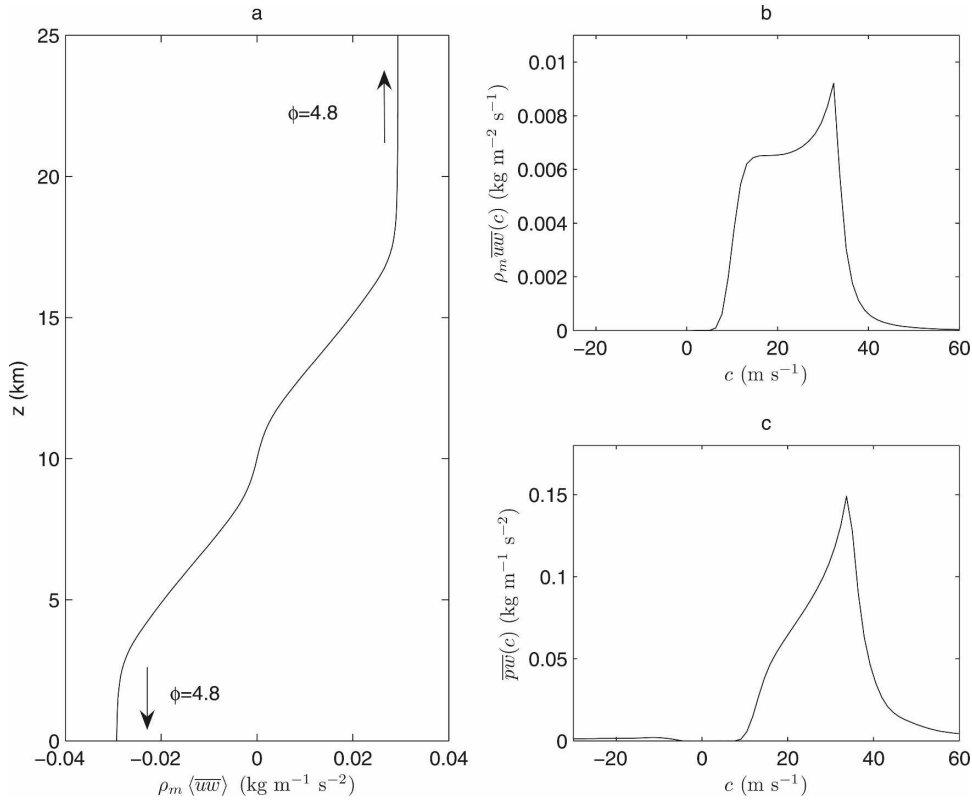


FIG. 6. (a) Distribution with height of the steady-state ensemble mean momentum flux $\rho\langle\bar{u}w\rangle$ for $k = 1$, $Ri = 16$, and velocity profile (10). As in Fig. 4, ϕ is the ensemble mean energy flux $\langle\bar{p}w\rangle$ calculated at $z = 0$ and $z = 2$ (20 km) and scaled by the corresponding flux $\langle\bar{p}w_0\rangle$ in the absence of a mean flow. Also shown is distribution with phase speeds of (b) $\rho\bar{u}w$ and (c) $\bar{p}w$ calculated at $z = 2.5$ (25 km).

is the dynamical operator, \mathbf{F} gives the spatial distribution of the forcing, and \mathbf{f} is a vector of δ correlated Gaussian white-noise processes of the form

$$\langle f_i(t_1)f_j(t_2) \rangle = \delta_{ij}\delta(t_1 - t_2). \tag{8}$$

As a result, each spatial forcing distribution specified by the columns of \mathbf{F} is equally and independently excited. For spatially uncorrelated forcing, we choose the columns of \mathbf{F} to be $\hat{H}(z) \sin[n\pi(z - 1)]$ and $\hat{H}(z) \cos[n\pi(z - 1)]$ for $n = 1, 2, \dots$, where

$$\hat{H}(z) = \begin{cases} e^{-40(z-0.4)^2}, & z < 0.4 \\ 1, & 0.4 \leq z \leq 1.6 \\ e^{-40(z-1.6)^2}, & z > 1.6 \end{cases} \tag{9}$$

is a tapered hat function restricting the forcing to the jet region. The forcing distribution is pass-banded at $n = 28$ to avoid exciting unresolved scales. Numerical tests with increased resolution showed that the results presented in this section are not sensitively dependent on the choice of n . The stochastic forcing rate for each zonal wavenumber is 0.1 W m^{-2} ; this forcing was cho-

sen so that the resulting variance in a motionless atmosphere equals the lower-tropospheric and stratospheric variance reported in Nastrom and Gage (1985) when integrated over all horizontal wavelengths.

The nondimensional velocity profile $U(z)$ given by

$$U(z) = e^{-[(z-1)/\delta z]^2} \tag{10}$$

is shown in Fig. 1. A sponge layer at the upper and lower boundaries implemented by Rayleigh damping (details of which are given in Part I), enforces radiation conditions. A small amount of diffusion is also introduced ($Re_s = 10^6$) to serve as a sink for energy transferred to unresolved scales.

The resulting ensemble mean steady-state fluxes can be calculated from integration of $\bar{u}w(\omega)$ and $\bar{p}w(\omega)$ over all frequencies:

$$[\langle\bar{u}w\rangle, \langle\bar{p}w\rangle] = \frac{1}{2\pi} \int_{-\infty}^{\infty} [\bar{u}w(\omega), \bar{p}w(\omega)] d\omega. \tag{11}$$

The corresponding equation in the discretized formulation is

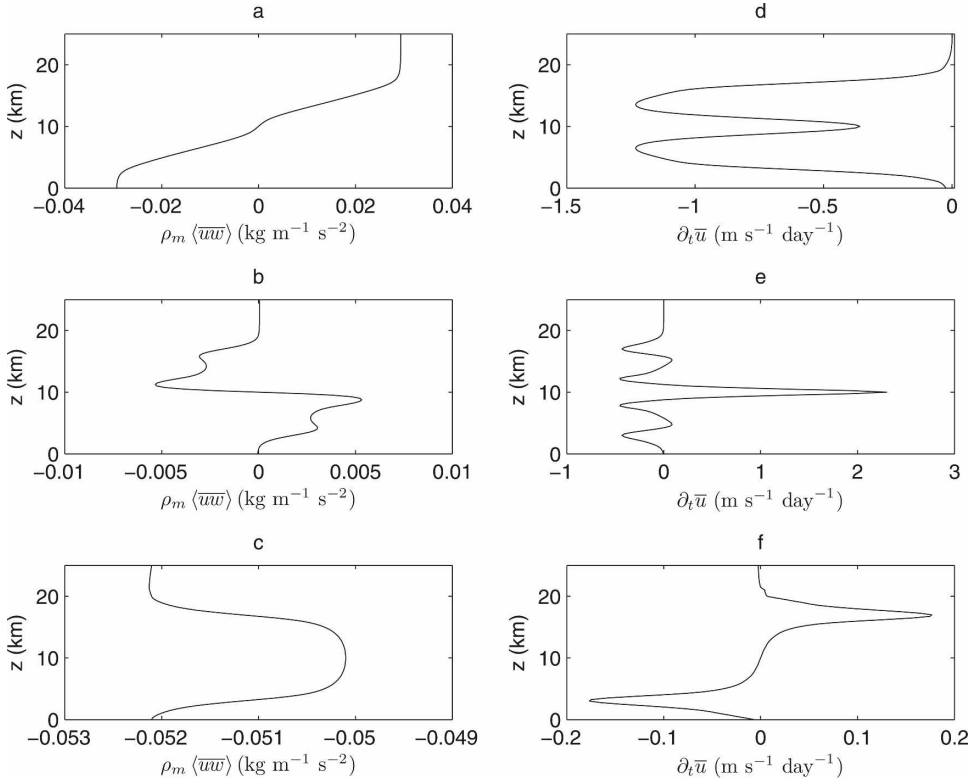


FIG. 7. Distribution with height of the steady-state ensemble mean momentum flux $\rho\langle\bar{u}\bar{w}\rangle$ for velocity profile (10) and for (a) $k = 1$, (b) $k = 20$, and also for (c) the stochastically forced finite shear layer studied in Part I with zonal wavenumber $k = 1$. Also shown is the corresponding flux divergence distribution with height for (d) $k = 1$, (e) $k = 20$, and (f) the finite shear layer. The Richardson number is $Ri = 16$.

$$\begin{aligned}
 & [\langle\mathbf{u}\mathbf{w}^\dagger\rangle, \langle\mathbf{p}\mathbf{w}^\dagger\rangle] \\
 &= \frac{1}{2\pi} \int_{-\infty}^{\infty} \{ \text{diag}[\mathbf{U}\mathbf{R}(\omega)\mathbf{F}\mathbf{F}^\dagger\mathbf{R}^\dagger(\omega)\mathbf{W}^\dagger], \\
 & \text{diag}[\mathbf{P}\mathbf{R}(\omega)\mathbf{F}\mathbf{F}^\dagger\mathbf{R}^\dagger(\omega)\mathbf{W}^\dagger] \} d\omega \quad (12)
 \end{aligned}$$

where diag denotes the diagonal elements of a matrix (a derivation of the above equation can be found in Part I) and \dagger denotes the Hermitian transpose. Alternatively, these fluxes can be obtained from the correlation matrix \mathbf{C} :

$$\mathbf{C} = \langle\mathbf{x}\mathbf{x}^\dagger\rangle = \int_0^t e^{\mathbf{A}(t-s)}\mathbf{F}\mathbf{F}^\dagger e^{\mathbf{A}^\dagger(t-s)} ds. \quad (13)$$

In steady state and for \mathbf{A} with all eigenvalues having negative real part, the asymptotic \mathbf{C}_∞ solves the Lyapunov equation:

$$\mathbf{A}\mathbf{C}_\infty + \mathbf{C}_\infty\mathbf{A}^\dagger = -\mathbf{F}\mathbf{F}^\dagger. \quad (14)$$

Pressure \mathbf{p} and horizontal and vertical velocities \mathbf{u} , \mathbf{w} can be expressed in terms of the state vector \mathbf{x} via linear

operators \mathbf{P} , \mathbf{U} , and \mathbf{W} (thus $\mathbf{p} = \mathbf{P}\mathbf{x}$, $\mathbf{u} = \mathbf{U}\mathbf{x}$ and $\mathbf{w} = \mathbf{W}\mathbf{x}$) yielding the following expressions for the momentum and energy fluxes respectively:

$$\langle\mathbf{u}\mathbf{w}^\dagger\rangle = \text{diag}(\mathbf{U}\langle\mathbf{x}\mathbf{x}^\dagger\rangle\mathbf{W}^\dagger) = \text{diag}(\mathbf{U}\mathbf{C}_\infty\mathbf{W}^\dagger), \quad (15)$$

$$\langle\mathbf{p}\mathbf{w}^\dagger\rangle = \text{diag}(\mathbf{P}\langle\mathbf{x}\mathbf{x}^\dagger\rangle\mathbf{W}^\dagger) = \text{diag}(\mathbf{P}\mathbf{C}_\infty\mathbf{W}^\dagger). \quad (16)$$

The distribution of $\langle\bar{u}\bar{w}\rangle$ with height is shown in Fig. 6a, and the similarity with the flux distribution shown in Fig. 4a indicates the dominance of type II waves for spatially uncorrelated forcing as well. Moreover, the enhanced energy fluxes ($\phi = 4.8$) are a clear manifestation of the dynamical effect of the mean flow in amplifying type II waves with phase lines tilting against the shear.

Inspection of the distribution of $\bar{u}\bar{w}$ and $\bar{p}\bar{w}$ with phase speeds shown in Fig. 6 reveals that waves with dimensional phase speeds in the range $16 < c < 36 \text{ m s}^{-1}$ carry most of the energy and momentum out of the jet and likely play an important role in driving the upper-atmosphere circulation by depositing this mo-

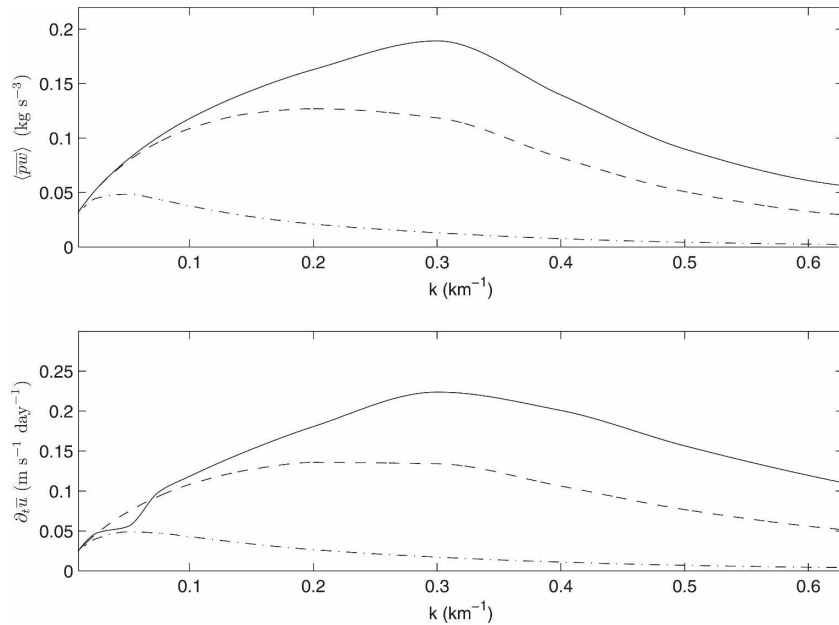


FIG. 8. (top) Ensemble mean energy flux $\langle \overline{p\overline{w}} \rangle$ at $z = 2.5$ (25 km) as a function of zonal wavenumber k for uncorrelated forcing (solid line), for autocorrelation time of $t_c = 2$ min (dashed line), and $t_c = 10$ min (dash-dot line). The velocity profile is (10) and the Richardson number is $\text{Ri} = 16$. (bottom) The corresponding mean momentum flux divergence in the region of the jet.

momentum as they break at higher altitudes.² This momentum transport away from the jet also has implications for the tropospheric and lower-stratospheric flow. The momentum flux divergence modifies the background flow, so that a mean velocity acceleration is induced according to $\partial_t \overline{u} = -\partial_z \overline{u\overline{w}}$. The resulting mean flow tendency for the steady-state momentum flux distribution shown in Fig. 6a is plotted in Fig. 7d and shows a large deceleration reaching a maximum in the wings of the jet. There is almost no acceleration due to flux divergence in the vicinity of the maximum of the jet wind speed, as the momentum deposited by trapped waves balances the momentum carried away from the jet by radiating waves in that region. The net result on averaging over the jet is a deceleration of $(1/2) \int_0^2 \partial_t \overline{u} dz = -0.7 \text{ m s}^{-1} \text{ day}^{-1}$ for horizontal wavelength $\lambda_x = 62.8 \text{ km}$. The mechanism of deceleration by radiation of momentum flux can be verified by looking at the extreme case of very large horizontal wavenumbers for which most of the wave activity is in type I waves, which are trapped inside the jet (see upper panel of Fig. 2). The $\langle \overline{u\overline{w}} \rangle$ distribution with height is plotted in Fig. 7b for $k = 20$ and the resulting mean flow tendency is

shown in Fig. 7e. We see a strong acceleration in the vicinity of the jet axis flanked by regions of deceleration and acceleration in the wings of the jet, yielding the required zero average wave-induced force. The energy fluxes and the mean flow tendency shown as a function of zonal wavenumber in Fig. 8 exhibit a maximum at wavenumber $k = 3$. For larger wavenumbers most of the wave activity is trapped in the jet as discussed above and lower wavenumbers are attenuated locally by the small amount of diffusion in the model because of their small group velocity. To estimate the force exerted on the jet, we integrate over all horizontal wavelengths in the range $\lambda_x \in [10, 628] \text{ km}$ to obtain a deceleration of $1 \text{ m s}^{-1} \text{ day}^{-1}$ for the stochastic forcing rate of 0.1 W m^{-2} .

The shape of the jet plays an important role in determining the sign of momentum flux radiated away from each side of the jet. To demonstrate this, we obtained the flux divergence for the case of the stochastically forced shear layer jet studied in Part I. The resulting momentum flux and flux divergence distributions with height are shown in Figs. 7c,f. The sign of radiated momentum is the same for both sides, producing a “dipole structure” of equal acceleration and deceleration at the upper and lower parts of the shear region respectively. The net flux divergence is zero and

² A more complete discussion about typical midlatitude jet structures will follow in section 5.

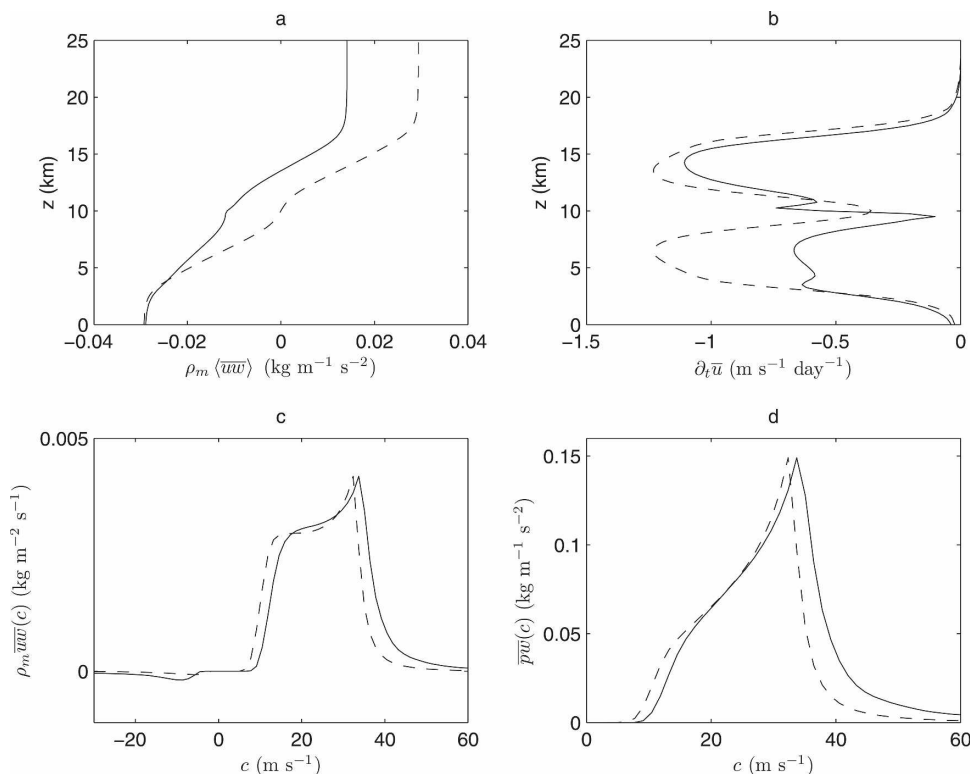


FIG. 9. (a) Steady-state ensemble mean momentum flux $\rho\langle\overline{uw}\rangle$ and (b) the corresponding flux divergence as a function of z for N^2 profile (17) and velocity profile (10). The corresponding distributions for a constant N^2 are plotted for reference (dashed lines). The Richardson number is $Ri = 16$ and $k = 1$. Phase speed spectra for (c) $\rho\overline{uw}(c)$ and (d) $\overline{pw}(c)$. The corresponding distribution of fluxes for a constant N^2 normalized to have the same maximum amplitude as in this case is also plotted (dashed lines) for reference.

the tendency is to reinforce rather than weaken the shear.

4. Sensitivity tests

The above calculations were performed for an idealized situation in which the buoyancy frequency is taken to be constant for the whole domain and the forcing is assumed to be purely thermal and temporally uncorrelated. Sensitivity studies, relaxing the above assumptions, are presented in this section.

Assuming the forcing to be purely thermal accounts only for buoyancy excitation, while other sources also force vorticity. These include shear-induced turbulence, unbalanced flows undergoing adjustment, wave breaking, and wave-wave interactions. We are interested in exploring qualitative changes in response to sources other than thermal without focusing overmuch on the considerable variability in source characteristics and so we choose the forcing to stochastically induce vorticity with the same forcing rate and the same spatial and temporal correlation as in the thermal forcing case. Ensemble mean flux distributions and phase speed spectra

proved to be insensitive to these changes in the forcing with only small quantitative differences of about 2% in the fluxes carried away from the jet.

Changes in static stability across the tropopause can be modeled by the buoyancy frequency profile

$$N^2 = N_0^2\{2.5 + 1.5 \tanh[(z - 1)/0.2]\} \quad (17)$$

that is constant throughout the troposphere with a two-fold increase at the tropopause. The calculations were repeated, and in Fig. 9 the resulting vertical distribution of momentum flux and flux divergence are shown. The symmetry of vertical momentum transport is broken as the momentum carried upward is reduced, but the jet deceleration is robust with larger drag occurring in this case in the lower stratosphere. Also note that \overline{uw} and \overline{pw} shown as functions of phase speed in Figs. 9c,d, are weakly influenced by the change in static stability with a small shift of the peak to a higher phase speed as waves acquire larger phase speeds for higher static stability.

In Part I, we found that increase in the temporal correlation of the forcing had a profound effect on the

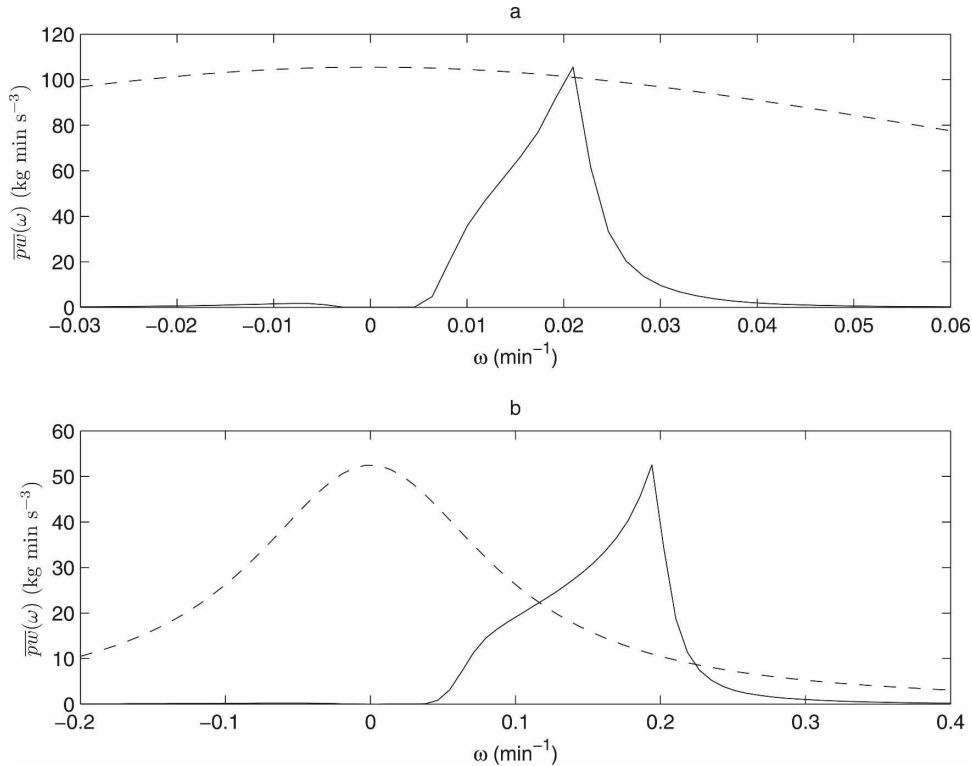


FIG. 10. Distribution of $\overline{p\overline{w}}$ with frequencies ω for (a) $k = 0.1$ (solid line) and (b) $k = 1$ (solid line). The fluxes are calculated at $z = 2.5$ (25 km), the Richardson number is $Ri = 16$, and the velocity profile used is given in (10). The power spectrum of the temporally correlated forcing $F(\omega) = \alpha^2/(\alpha^2 + \omega^2)$, where $\alpha = 1/10 \text{ min}^{-1}$, is also plotted (dashed line) for reference and is normalized to have at $\omega = 0$ the maximum value of $\overline{p\overline{w}}$ in each case.

emitted fluxes, especially for large zonal wavenumbers. The dependence of the fluxes and the resulting deceleration of the jet on the autocorrelation time of the forcing t_c is shown in Fig. 8 for $t_c = 2 \text{ min}$ and $t_c = 10 \text{ min}$. For low zonal wavenumbers there is adequate forcing power at the range of frequencies of maximum response as shown in Fig. 10a, where the $\overline{p\overline{w}}$ frequency spectra are plotted for $k = 0.1$ along with the power spectrum of the forcing $F(\omega) = 1/(1 + t_c^2\omega^2)$. As a result, the fluxes e -fold for autocorrelation times of the order of $t_c = 1 \text{ h}$, in contrast to the higher zonal wavenumber case (Fig. 10b, where the $\overline{p\overline{w}}$ frequency spectra is plotted for $k = 1$), where significant power at the dominant response frequencies is not available and the outgoing fluxes and the force exerted on the jet are reduced.

5. Implications for the Northern and Southern Hemisphere midlatitude jets: Discussion

Mean wind profiles for the winter and summer midlatitude jets taken from the Cooperative Institute for

Research in the Atmosphere (CIRA) reference atmosphere (Fleming et al. 1990) are shown in Fig. 11. The observations are fit with Gaussian functions of height:

$$U_{\text{winter}}(z) = 0.9 \exp[-(z - 1.25)^2/0.75] + 2 \exp[-(z - 6.7)^2/8] \quad (18)$$

for the winter and

$$U_{\text{summer}}(z) = \exp[-(z - 1.31)^2/0.75] - 2.5 \exp[-(z - 7)^2/14] \quad (19)$$

for the summer jet, also shown in Fig. 11. The summer jet is similar within the troposphere and stratosphere to the Gaussian mean wind profile used in the previous sections (Fig. 11). In contrast, the winter jet exhibits a local minimum $U_{\text{min}} = 12 \text{ m s}^{-1}$ at $z = 25 \text{ km}$ enabling further propagation of waves with phase speeds in the range $[0, U_{\text{min}}]$. This is illustrated by the presence of waves with phase speeds $0 < c < 12 \text{ m s}^{-1}$ in the momentum phase speed spectra plotted in Fig. 12a. It is

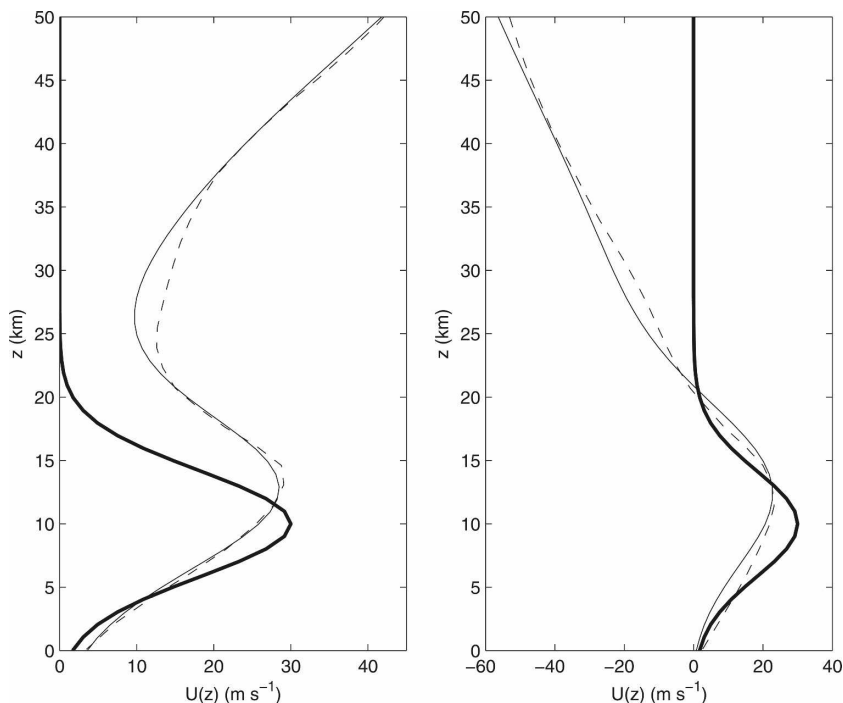


FIG. 11. (left) Zonal mean wind profile for 40°N January from CIRA (dashed line). The solid line is a smooth fit to the observations denoted $U_{\text{winter}}(z)$ (see text for details). (right) Zonal mean wind profile for 40°S January from CIRA (dashed line). The solid line is a smooth fit to the observations denoted $U_{\text{summer}}(z)$ (see text for details). The thick line in both panels is the profile shown in Fig. 1.

worth noting that if they do not break convectively at a lower height, these waves carrying westward momentum can propagate into the mesosphere to drive the mesospheric circulation, unlike waves with larger phase speeds transporting westerly momentum that are bounded by their critical levels to the stratosphere.

The solution for the summer jet is not very different from that found for the Gaussian jet studied in section 3, with a large outgoing westward momentum flux that will be deposited at wave-breaking altitudes within the upper stratosphere and mesosphere and induce a decelerative force there (decelerative in the sense that the force opposes the local mean wind). In both summer and winter jets the wave flux divergence decelerates the tropospheric and lower-stratospheric mean flow, as shown in Figs. 12c,d.

These results can now be related to observational and modeling studies. Sutherland and Peltier (1995) also considered the possibility of the mean flow being affected by emission rather than absorption of waves. They investigated the conditions necessary for a shear instability to effectively excite inertia-gravity waves and examined the robustness of the mechanism under different conditions. They found that westward gravity waves are preferentially excited and radiated away, re-

sulting in a deceleration of the tropospheric jet. The results of our work differ in that our waves are stochastically forced, and shear instability and its required structure are not assumed.

During the past decade, a wide variety of techniques have been used to observe the seasonal and geographical variations in gravity wave activity. These include rocketsonde measurements (Eckermann 1995), radiosonde soundings (Allen and Vincent 1995), and satellite observations (Fetzer and Gille 1994; Wu and Waters 1996; Tsuda et al. 2000; McLandress et al. 2000) that have the advantage of providing a global coverage. Although each of these techniques can detect only a small part of the gravity wave spectrum, most show a correlation of gravity wave activity with the midlatitude jet, with maximum variance during the season of largest mean wind velocities.

Alexander (1998) and McLandress et al. (2000) using ray tracing in conjunction with an assumed source of waves, showed that wave refraction and observational filtering result to the observed patterns of variance. In section 2 it was shown that the interaction of excited perturbations with the mean flow augments the source of wave action arising from a spatially localized forcing, yielding larger momentum and energy fluxes for stron-

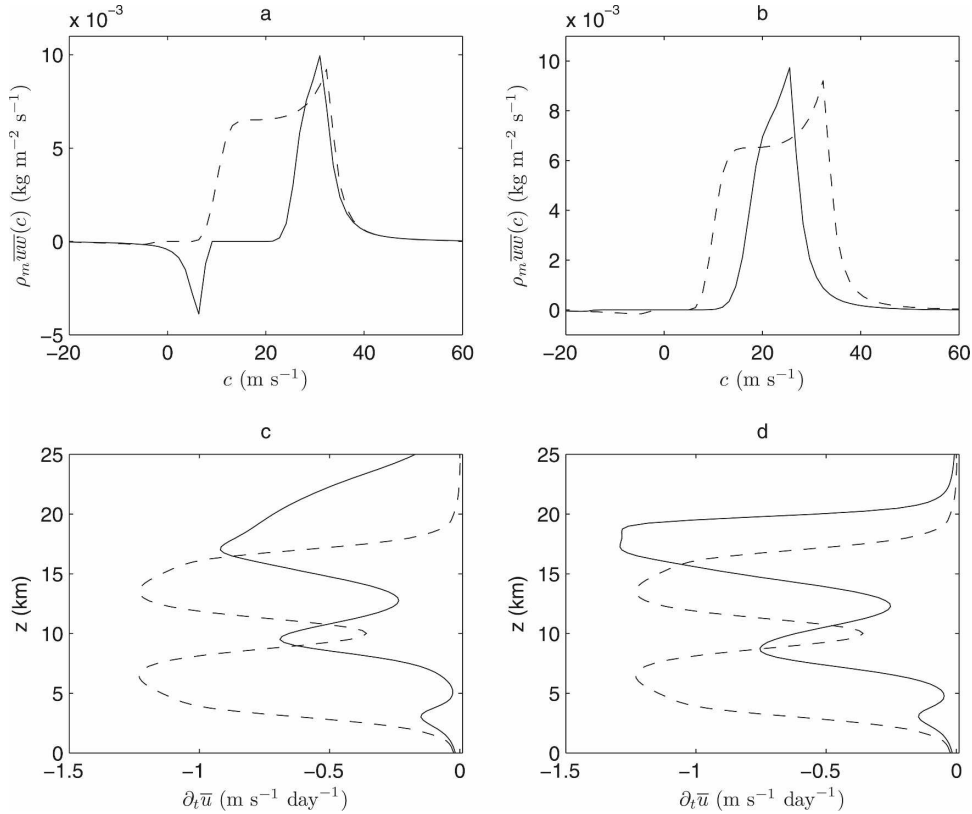


FIG. 12. Distribution of $\rho \overline{uw}$ with wave phase speeds at $z = 2.5$ (25 km) for the (a) winter jet and (b) summer jet. The corresponding distribution of fluxes for the profile in Fig. 1 (dashed line) is shown for reference. Also shown is the momentum flux divergence distribution with height for the (c) winter jet and (d) summer jet. The corresponding distribution for the profile in Fig. 1 (dashed line) is shown for reference. The Richardson number in all calculations is $Ri = 16$ and zonal wavenumber is $k = 1$.

ger shear. This was also verified for the distributed, spatially uncorrelated forcing and is illustrated in Fig. 13 where the ensemble mean momentum fluxes at $z = 2.5$ are plotted as a function of the maximum wind speed of the jet. If instead of momentum flux we measure variance in the overlying region we find the same functional dependence on the maximum wind speed of the jet. This result suggests that the observed correlation of gravity wave activity with wind velocity is at least in part a result of wave–mean flow interactions in the presence of forcing, a mechanism not contained in models that follow ray paths of a spectrum of waves.

This line of thinking suggests identifying forcing distributions that yield the greatest response, that is, the properly defined stochastic optimals. We optimized energy fluxes at $z = 25$ km and variance within the overlying region. Since there were minor differences in the stochastic optimals when optimizing for variance and energy fluxes, the results presented in this section correspond to the forcing distributions yielding the greatest response in terms of energy fluxes. These can be

calculated by eigenanalysis of the matrix \mathbf{B}_∞ that is the solution to the Lyapunov equation:

$$\mathbf{A}_m^\dagger \mathbf{B}_\infty + \mathbf{B}_\infty \mathbf{A}_m + \mathbf{Pw} = \mathbf{0}, \tag{20}$$

where

$$\mathbf{Pw} = (\mathbf{M}^{-1/2})^\dagger \mathbf{W}^\dagger \mathbf{M}_T \mathbf{P} \mathbf{M}^{-1/2}, \tag{21}$$

$$\mathbf{A}_m = \mathbf{M}^{1/2} \mathbf{A} \mathbf{M}^{-1/2}, \tag{22}$$

and \mathbf{M}_T is a metric, whose only nonzero element is the one corresponding to $z = 2.5$ (a formal derivation can be found in Part I). Figure 14 shows the structure of the first stochastic optimal for the summer jet and the winter jet. In both cases, the optimal forcing corresponds to structures just above the maximum of the jet, indicating that the vicinity of the jet axis is a region that produces the greatest contribution to the emitted gravity wave energy fluxes.

6. Conclusions

Mechanisms determining the statistical equilibrium gravity wave fluxes in atmospheric jets were studied in

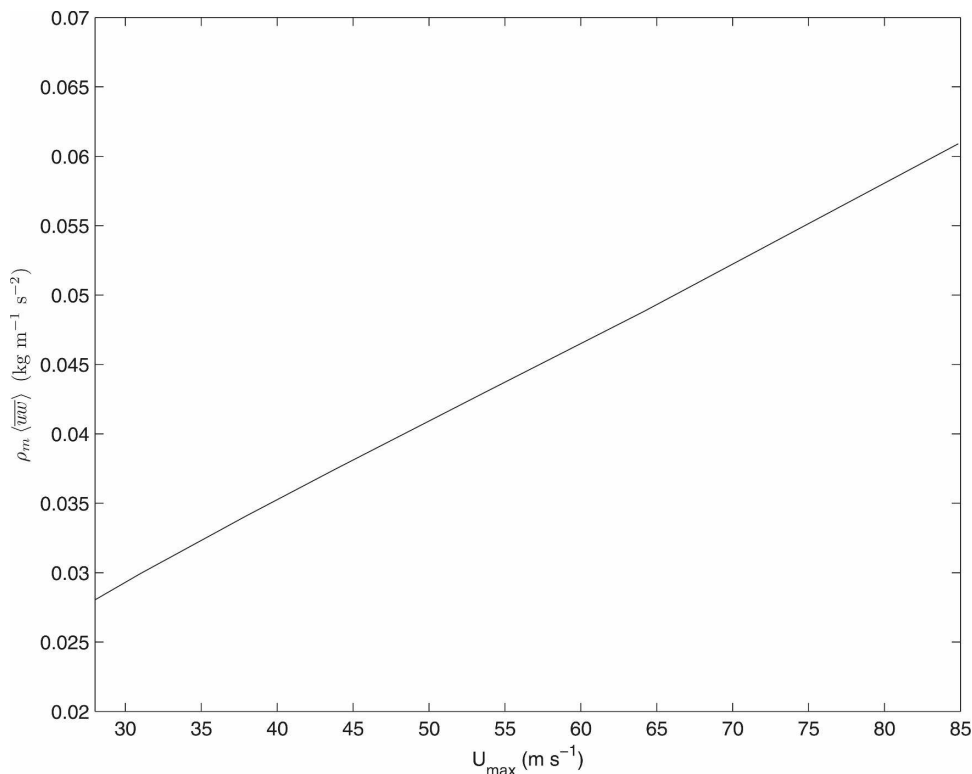


FIG. 13. Ensemble mean momentum flux $\rho \langle \bar{u}\bar{w} \rangle$ calculated at $z = 2.5$ (25 km) as a function of the maximum wind speed of the jet U_{\max} for velocity profile (10). The zonal wavenumber is $k = 1$.

this paper, using tools provided by generalized stability theory. Nonnormality of the underlying linear dynamics was found to play an important role in processing the wave activity and selecting structures that dominate wave momentum and energy transport. To focus on the wave–mean flow interactions without introducing a biased forcing function, the waves were assumed to be excited by stochastic white-noise forcing.

A GST analysis of a stably stratified two-dimensional jet was performed. A Gaussian structure for the jet mean velocity profile was assumed with a maximum wind speed of 30 m s^{-1} at a 10-km height, and a typical tropospheric value was chosen for the static stability. First the jet was approximated by two shear layers allowing closed-form solutions, and in this simple model the response to a source harmonic in x and localized at the jet maximum as a delta function in z was obtained. Waves with short wavelength ($\lambda_x < 16 \text{ km}$) were found to be trapped inside the jet and to deposit their momentum and energy at their critical levels. In contrast, longer low intrinsic frequency waves produced outgoing momentum and energy transport. This behavior characterized the case of spatially and temporally uncorrelated forcing of the Gaussian jet as well. Wave radiation is likely to influence the middle atmosphere

circulation through momentum deposition as well as the tropospheric and stratospheric flows due to deceleration by momentum flux divergence. The induced deceleration was found to depend on the shape of the jet and on the horizontal wavelength of the excited waves with the fluxes and the resulting average deceleration reaching a maximum at horizontal wavelength $\lambda_x = 20 \text{ km}$. The deceleration is reduced when the stochastic forcing becomes sufficiently highly correlated in time. However, the reduction of wave fluxes and of the corresponding flux divergence depends on the horizontal wavenumber of the excited waves. Red-noise forcing was found to weakly excite waves with horizontal wavenumber larger than $k = 1$ ($\lambda_x = 63 \text{ km}$) while lower wavenumbers are relatively unaffected even for correlation times of the order of half an hour. There were no significant changes in the wave fluxes when we considered vorticity forcing instead of diabatic heating as the source of excitation, while the average drag was found to be slightly reduced by including the change of background static stability at the tropopause. Accordingly, the average deceleration of $1 \text{ m s}^{-1} \text{ day}^{-1}$ produced in the troposphere and lower stratosphere in the case of spatially and temporally uncorrelated forcing with forcing rate of 0.1 W m^{-2} for each zonal wave-

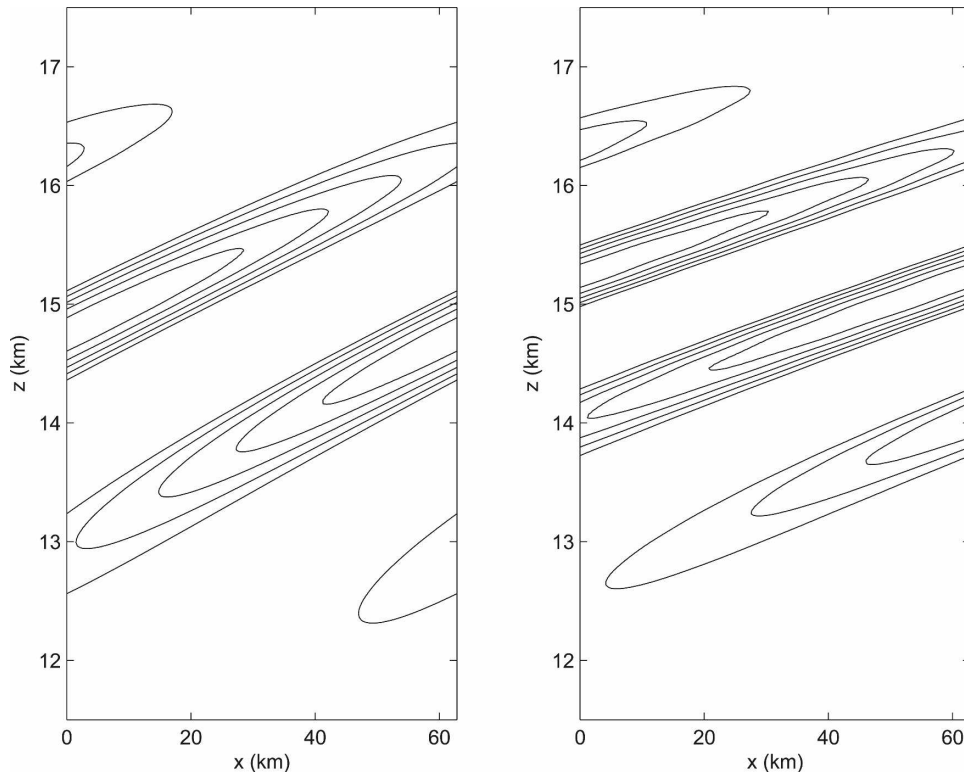


FIG. 14. (left) Structure of the first stochastic optimal forcing of the summer jet. This structure accounts for 16.5% of the resulting energy flux. (right) Structure of the first stochastic optimal forcing of the winter jet accounting for 16% of the energy flux. In both panels the Richardson number is $Ri = 16$ and the horizontal wavenumber is $k = 1$.

number is likely to be reduced in more realistic conditions. An open question that will be addressed in future work is how the jet equilibrates if we let it respond to the flow-consistent wave forcing and evolve the coupled wave field–mean flow system using a quasilinear adjustment scheme. Nevertheless, the deceleration appears to be significant, suggesting it be incorporated to improve parameterizations of gravity wave drag. This might be implemented by a stochastic buoyancy forcing in the troposphere.

The specific differences in response of the typical winter and summer midlatitude jets were also examined. Differences in mean flow effectively determine through critical-level filtering which gravity waves radiate away and are potentially able to reach the upper stratosphere and mesosphere. In the typical winter jet the local minimum of the wind within the stratosphere allows waves with phase speeds in the range $0 < c < 12 \text{ m s}^{-1}$ to propagate into the upper stratosphere, whereas the stratospheric easterlies in the typical summer jet allow only waves with phase speeds in the range $12 < c < 36 \text{ m s}^{-1}$, which carry westward momentum to propagate into the stratosphere. However, in all cases

emission of waves induces a momentum flux divergence resulting in a mean deceleration of the tropospheric and lower-stratospheric jet stream.

Finally, the link between enhanced gravity wave variance and high jet speed that is evident in observational studies was investigated. This observed link is traced not only to wave refraction and filtering of waves conserving wave action but also to nonnormal wave–mean flow interactions in conjunction with the distributed forcing that serves as a source of wave action. The structure of the calculated stochastic optimals reveals that the region above the jet axis produces the greatest contribution to the emission of gravity wave energy fluxes, when adequately excited.

Acknowledgments. The authors thank two anonymous reviewers for their useful comments and numerous suggestions, which helped to improve the manuscript. It is also a pleasure to acknowledge helpful discussions with Prof. Petros Ioannou. This work was supported by the National Science Foundation Grant ATM-0736022.

APPENDIX

Response for Zonal Wave Forcing Localized in the Vertical

We find the Green’s function for thermal forcing of the form

$$f_l(x, z, t) = \delta(z - z_\delta)e^{ikx}e^{-ikct}, \tag{A1}$$

where $z_\delta = 1.01$ for the calculations shown in Figs. 3 and 4 and $z_\delta = 1.5$ for the calculations shown in Fig. 5.

Introducing in (1a)–(1b) a monochromatic solution of the form $[\psi(x, z, t), \rho(x, z, t)] = [\hat{\psi}(z), \hat{\rho}(z)]e^{ikx}e^{-ikct}$ and eliminating $\hat{\rho}$ we obtain

$$\frac{d^2\hat{\psi}}{dz^2} + \left(\frac{\text{Ri}}{(U(z) - c\sqrt{\text{Ri}})^2} - \frac{d^2U}{dz^2} \frac{1}{(U(z) - c\sqrt{\text{Ri}})} - k^2 \right) \hat{\psi} = \frac{\text{Ri}}{ik(U(z) - c\sqrt{\text{Ri}})^2} \delta(z - z_\delta), \tag{A2}$$

the solution of which is

$$\hat{\psi}(z, \tilde{c}) = \begin{cases} He^{il_u(z-z_0)}, & \text{for } z \geq 2 \\ F\sqrt{k(z-2+\tilde{c})}I_\mu[k(z-2+\tilde{c})] + G\sqrt{k(z-2+\tilde{c})}I_{-\mu}[k(z-2+\tilde{c})], & \text{for } z_\delta \leq z < 2 \\ D\sqrt{k(\tilde{c}-z)}I_\mu[k(\tilde{c}-z)] + E\sqrt{k(\tilde{c}-z)}I_{-\mu}[k(\tilde{c}-z)], & \text{for } 1 \leq z < z_\delta \\ B\sqrt{k(\tilde{c}-z)}I_\mu[k(\tilde{c}-z)] + C\sqrt{k(\tilde{c}-z)}I_{-\mu}[k(\tilde{c}-z)], & \text{for } 0 \leq z < 1 \\ Ae^{il_z z}, & \text{for } z < 0, \end{cases} \tag{A3}$$

where $\tilde{c} = c\sqrt{\text{Ri}}$, l_l and l_u are both the square root of $1/c^2 - k^2$, having $\Re(l_l)c > 0$, $\Im(l_l) < 0$, $\Re(l_u)c < 0$, $\Im(l_u) > 0$, respectively, in order to satisfy boundedness or radiation conditions at $z \rightarrow \mp\infty$, $\mu = \sqrt{1/4 - \text{Ri}}$, and $I_{\pm\mu}$ is the modified Bessel function of the second kind of order μ .

Continuity of displacement and pressure at $z = 0, z =$

1, and $z = 2$ and integrating twice (A2) from $z = z_\delta^-$ to $z = z_\delta^+$ yields eight algebraic equations for the amplitudes in (A3), which are expressed in matrix form as

$$[\mathbf{B}_1, \mathbf{B}_2]\mathbf{Y} = \mathbf{B}_3, \tag{A4}$$

where $\mathbf{Y} = [A, B, C, D, E, F, G, H]^T$,

$$\mathbf{B}_1 = \begin{pmatrix} 1 & -a_+ & -a_- & 0 \\ il_l\tilde{c} & -k\tilde{c}\delta a_+ - a_+ & -k\tilde{c}\delta a_- - a_- & 0 \\ 0 & -b_+ & -b_- & b_+ \\ 0 & -k(1-\tilde{c})\delta b_+ + b_+ & -k(1-\tilde{c})\delta b_- + b_- & -k(1-\tilde{c})\delta b_+ + b_+ \\ 0 & 0 & 0 & -c_+ \\ 0 & 0 & 0 & -k\delta c_+ \\ 0 & 0 & 0 & 0 \\ 0 & 0 & 0 & 0 \end{pmatrix}, \tag{A5}$$

$$\mathbf{B}_2 = \begin{pmatrix} 0 & 0 & 0 & 0 & 0 \\ 0 & 0 & 0 & 0 & 0 \\ b_- & 0 & 0 & 0 & 0 \\ -k(1-\tilde{c})\delta b_- + b_- & 0 & 0 & 0 & 0 \\ -c_- & d_+ & d_- & 0 & 0 \\ -k\delta c_- & k\delta d_+ & k\delta d_- & 0 & 0 \\ 0 & -e_+ & -e_- & 1 & 0 \\ 0 & -k\tilde{c}\delta e_+ + e_+ & -k\tilde{c}\delta e_- + e_- & il_u\tilde{c} & 0 \end{pmatrix}, \tag{A6}$$

and

$$\mathbf{B}_3 = [0, 0, 0, 1/(ikc^2), 0, 0, 0, 0]^T. \quad (\text{A7})$$

The coefficients in the equations above are

$$a_{\pm} = -ie^{\mp iu\pi} \sqrt{z_l} I_{\pm\mu}(z_l), \quad b_{\pm} = \sqrt{z_u} I_{\pm\mu}(z_u),$$

$$c_{\pm} = \sqrt{z_f} I_{\pm\mu}(z_f), \quad d_{\pm} = c_{\pm}, \quad e_{\pm} = a_{\pm},$$

$$\delta a_{\pm} = ie^{\mp iu\pi} \left[\frac{I_{\pm\mu}(z_l)}{2\sqrt{z_l}} + \sqrt{z_l} \frac{dI_{\pm\mu}}{dz} \Big|_{z_l} \right],$$

$$\delta b_{\pm} = \frac{I_{\pm\mu}(z_u)}{2\sqrt{z_u}} + \sqrt{z_u} \frac{dI_{\pm\mu}}{dz} \Big|_{z_u},$$

$$\delta c_{\pm} = \frac{I_{\pm\mu}(z_f)}{2\sqrt{z_f}} + \sqrt{z_f} \frac{dI_{\pm\mu}}{dz} \Big|_{z_f}, \quad \delta d_{\pm} = \delta c_{\pm},$$

$$\delta e_{\pm} = -\delta a_{\pm}, \quad z_l = k\tilde{c}, \quad z_u = k(1 - \tilde{c}),$$

$$z_f = k(z_{\delta} - \tilde{c}),$$

when $0 < \tilde{c} < 2 - z_{\delta}$. When $2 - z_{\delta} < \tilde{c} < 1$, the coefficients are

$$a_{\pm} = -ie^{\mp iu\pi} \sqrt{z_l} I_{\pm\mu}(z_l), \quad b_{\pm} = \sqrt{z_u} I_{\pm\mu}(z_u),$$

$$c_{\pm} = -ie^{\mp iu\pi} \sqrt{z_f} I_{\pm\mu}(z_f), \quad d_{\pm} = \sqrt{z_f} I_{\pm\mu}(z_f),$$

$$e_{\pm} = \sqrt{z_l} I_{\pm\mu}(z_l),$$

$$\delta a_{\pm} = ie^{\mp iu\pi} \left[\frac{I_{\pm\mu}(z_l)}{2\sqrt{z_l}} + \sqrt{z_l} \frac{dI_{\pm\mu}}{dz} \Big|_{z_l} \right],$$

$$\delta b_{\pm} = \frac{I_{\pm\mu}(z_u)}{2\sqrt{z_u}} + \sqrt{z_u} \frac{dI_{\pm\mu}}{dz} \Big|_{z_u},$$

$$\delta c_{\pm} = ie^{\mp iu\pi} \left[\frac{I_{\pm\mu}(z_f)}{2\sqrt{z_f}} + \sqrt{z_f} \frac{dI_{\pm\mu}}{dz} \Big|_{z_f} \right],$$

$$\delta d_{\pm} = - \left[\frac{I_{\pm\mu}(z_f)}{2\sqrt{z_f}} + \sqrt{z_f} \frac{dI_{\pm\mu}}{dz} \Big|_{z_f} \right],$$

$$\delta e_{\pm} = \frac{I_{\pm\mu}(z_l)}{2\sqrt{z_l}} + \sqrt{z_l} \frac{dI_{\pm\mu}}{dz} \Big|_{z_l}, \quad z_l = k\tilde{c},$$

$$z_u = k(1 - \tilde{c}), \quad z_f = k(\tilde{c} - z_{\delta}).$$

In case $1 < \tilde{c}$, they are

$$a_{\pm} = \sqrt{z_l} I_{\pm\mu}(z_l), \quad b_{\pm} = \sqrt{z_u} I_{\pm\mu}(z_u),$$

$$c_{\pm} = \sqrt{z_f} I_{\pm\mu}(z_f), \quad d_{\pm} = c_{\pm}, \quad e_{\pm} = \sqrt{z_l} I_{\pm\mu}(z_l),$$

$$\delta a_{\pm} = - \left(\frac{I_{\pm\mu}(z_l)}{2\sqrt{z_l}} + \sqrt{z_l} \frac{dI_{\pm\mu}}{dz} \Big|_{z_l} \right),$$

$$\delta b_{\pm} = - \left(\frac{I_{\pm\mu}(z_u)}{2\sqrt{z_u}} + \sqrt{z_u} \frac{dI_{\pm\mu}}{dz} \Big|_{z_u} \right),$$

$$\delta c_{\pm} = - \left(\frac{I_{\pm\mu}(z_f)}{2\sqrt{z_f}} + \sqrt{z_f} \frac{dI_{\pm\mu}}{dz} \Big|_{z_f} \right), \quad \delta d_{\pm} = \delta c_{\pm},$$

$$\delta e_{\pm} = \frac{I_{\pm\mu}(z_l)}{2\sqrt{z_l}} + \sqrt{z_l} \frac{dI_{\pm\mu}}{dz} \Big|_{z_l}, \quad z_l = k\tilde{c},$$

$$z_u = k(\tilde{c} - 1), \quad z_f = k(\tilde{c} - z_{\delta}).$$

Otherwise they are

$$a_{\pm} = \sqrt{z_l} I_{\pm\mu}(z_l), \quad b_{\pm} = \sqrt{z_u} I_{\pm\mu}(z_u),$$

$$c_{\pm} = \sqrt{z_f} I_{\pm\mu}(z_f), \quad d_{\pm} = c_{\pm}, \quad e_{\pm} = a_{\pm},$$

$$\delta a_{\pm} = \frac{I_{\pm\mu}(z_l)}{2\sqrt{z_l}} + \sqrt{z_l} \frac{dI_{\pm\mu}}{dz} \Big|_{z_l},$$

$$\delta b_{\pm} = \frac{I_{\pm\mu}(z_u)}{2\sqrt{z_u}} + \sqrt{z_u} \frac{dI_{\pm\mu}}{dz} \Big|_{z_u},$$

$$\delta c_{\pm} = \frac{I_{\pm\mu}(z_f)}{2\sqrt{z_f}} + \sqrt{z_f} \frac{dI_{\pm\mu}}{dz} \Big|_{z_f}, \quad \delta d_{\pm} = \delta c_{\pm},$$

$$\delta e_{\pm} = -\delta a_{\pm}, \quad z_l = -k\tilde{c}, \quad z_u = k(1 - \tilde{c}),$$

$$z_f = k(z_{\delta} - \tilde{c}).$$

The resulting momentum and energy fluxes are

$$\overline{uw}(\omega) = \frac{1}{2} \Re(\hat{u}\hat{w}^*) = \frac{1}{2} \Re(ik\partial_z \hat{\psi}\hat{\psi}^*) \quad (\text{A8})$$

and

$$\begin{aligned} \overline{p\overline{w}}(\omega) &= \frac{1}{2} \Re(\hat{p}\hat{w}^*) \\ &= \frac{1}{2} \Re \left[-(U/\sqrt{\text{Ri}} - c)\hat{u}\hat{w}^* + \frac{i}{k\sqrt{\text{Ri}}} \frac{dU}{dz} \hat{w}\hat{w}^* \right] \\ &= \frac{1}{2} \Re \left[-ik(U/\sqrt{\text{Ri}} - c)\partial_z \hat{\psi}\hat{\psi}^* \right], \end{aligned} \quad (\text{A9})$$

respectively.

REFERENCES

- Alexander, M. J., 1998: Interpretations of observed climatological patterns in stratospheric gravity wave variance. *J. Geophys. Res.*, **103**, 8627–8640.
- Allen, S. J., and R. A. Vincent, 1995: Gravity wave activity in the lower atmosphere: Seasonal and latitudinal variations. *J. Geophys. Res.*, **100**, 1327–1350.
- Bakas, N. A., and P. J. Ioannou, 2007: Momentum and energy transport by gravity waves in stochastically driven stratified flows. Part I: Radiation of gravity waves from a shear layer. *J. Atmos. Sci.*, **64**, 1509–1529.
- Eckermann, S. D., 1995: On the observed morphology of gravity-

- wave and equatorial-wave variance in the stratosphere. *J. Atmos. Terr. Phys.*, **57**, 105–134.
- Farrell, B. F., and P. J. Ioannou, 1996: Generalized stability theory. Part I: Autonomous operators. *J. Atmos. Sci.*, **53**, 2025–2030.
- Fetzer, E. J., and J. C. Gille, 1994: Gravity wave variance in LIMS temperatures. Part I: Variability and comparison with background winds. *J. Atmos. Sci.*, **51**, 2461–2483.
- Fleming, E. L., S. Chandra, J. J. Barnett, and M. Corney, 1990: Zonal mean temperature, pressure, zonal wind and geopotential height as functions of latitude. *Adv. Space Res.*, **10** (12), 11–59.
- McLandress, C., M. J. Alexander, and D. L. Wu, 2000: Microwave Limb Sounder observations of gravity waves in the stratosphere: A climatology and interpretation. *J. Geophys. Res.*, **105**, 11 947–11 967.
- Nastrom, G. D., and K. S. Gage, 1985: A climatology of atmospheric wavenumber spectra of wind and temperature observed by commercial aircraft. *J. Atmos. Sci.*, **42**, 950–960.
- Sutherland, B. R., 2000: Internal wave reflection in uniform shear. *Quart. J. Roy. Meteor. Soc.*, **126**, 3255–3286.
- , and W. R. Peltier, 1995: Internal gravity wave emission into the middle atmosphere from a model tropospheric jet. *J. Atmos. Sci.*, **52**, 3214–3235.
- Tsuda, T., M. Nishida, C. Rocken, and R. H. Ware, 2000: A global morphology of gravity wave activity in the stratosphere revealed by the GPS occultation data (GPS/MET). *J. Geophys. Res.*, **105**, 7257–7273.
- Wu, D. L., and J. W. Waters, 1996: Gravity-wave-scale temperature fluctuations seen by the UARS MLS. *Geophys. Res. Lett.*, **23**, 3289–3292.